Universitatea Alexandru Ioan Cuza, Facultatea de Fizică

$BiFeO_3$ - $CoFe_2O_4$ nanostructured multiferroic thin films

Sergiu Mihai Stratulat

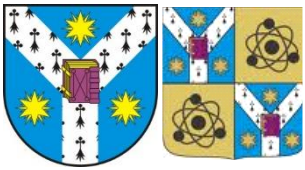

Supervisor
prof. dr. Ovidiu Florin Călţun

Supervisor
dr. Marin Alexe

Iași, 2013

Contents

Abstract *1*

Acknowledgements *3*

Introduction *6*

Chapter I. Magnetoelectric materials *10*

I.1 Single-phase magnetoelectrics **11**

I.2 Hmagnetoelectric heterostructures **12**

I.2.1 Common materials for magnetoelectric thin films heterostructures 16

I.3 Bismuth ferrite – $BiFeO_3$ (BFO) **17**

I.3.1 Ferroelectric properties 19

I.3.2 Magnetic properties 20

I.3.3 Electric properties 21

I.3.4 Magnetoelectric properties 21

I.4 Aplications **22**

Chapter II. Pulsed laser deposition of thin films *23*

II.1 Target-laser interaction **25**

II.2 Thin films' growth modes **28**

II.3 Mechanisms and theories concerning thin films' growth **30**

II.3.1 Adsorbtion theory 30

II.3.2 Thermodinamic theory 31

II.3.3 Atomic or statistical theory 32

II.4 Epitaxial growth **33**

Chapter III. Experimental techniques *36*

III.1 Atomic force miscroscopy **37**

III.2 scanning electron miscroscopy **40**

III.3 Magnetocapacitance measurements 40

III.4 Raman spectroscopy 42

Chapeter IV. Alternative route for obtaining NiFe2O4 thin films by PLD 44

IV.1 Introduction 45

IV.2 Film deposition 46

IV.3 Structural characterization 47

Chapter V. Nanostructured multiferroic system BiFeO3 – CoFe2O4 .. 53

V.1 Introduction 54

V.2 Synthesis method 56

V.3 Structural characterization 59

V.4 Functional characterization 65

V.5 Magnetoelectric coupling 69

Conclusions 78

References 80

Communications and publications list: 86

Introduction

The term “multiferroic” defines materials with at least two ferroic orders: magnetism, ferroelectricity and ferroelasticity. Present days, this notion is widely used to refer to the existence of magnetism and ferroelectricity and the coupling between them. This magnetoelectric coupling offers the possibility of magnetically controlling the electric polarization and electrically controlling the magnetization [1,2] (figure 1), with applications that may arise in industries such as that of sensors, transducers, magnetic memories, etc. [3,4].

This study was focused on the growth and characterization of magnetoelectric heterostructures comprising $BiFeO_3$ and $CoFe_2O_4$. We chose the materials due to their individual properties, which make them suitable for these kind of heterostructures (e.g. high piezoelectric coefficient, high magnetostriction), and due to the synergy between them (e.g. similar crystalline structure, low immiscibility). The aim of this work was the vertical type of heterostructures (1-3 connectivity) consisting of magnetic pillars embedded in a ferroelectric matrix. A special focus was set on developing a process that would produce a highly ordered arrangement of these pillars.

The thesis is structured on 5 chapters: chapter I offers a broad overview on magnetoelectric materials and also some properties of bismuth ferrite; chapter II deals with the growth of thin films through pulsed laser deposition; in chapter III, the characterization techniques are shortly described; chapter IV presents the results for the alternative process of $NiFe_2O_4$ thin film growth; chapter V is detailing the results for the growth and characterization of vertical magnetoelectric heterostructures $BiFeO_3$ – $CoFe_2O_4$.

Chapter I. Magnetoelectric materials

I.1 Single-phase multiferroic materials

The interest in single-phase multiferroics is having both magnetism and ferroelectricity, and also the coupling between them. The biggest drawback is the mutual exclusion of the mechanism for magnetism and the classical one for ferroelectricity. Thus, for further study, several novel ferroelectricity origins have been taken into account that would permit the existence of magnetic order.

I.2 Magnetoelectric heterostructures

The low number of single-phase multiferroics led to the development of magnetoelectric composite systems. In this case, the coupling is a product property, obtained by interfacing two distinct materials, a magnetic and a ferroelectric one. An important notion for these heterostructures is the concept of phase connectivity [25], which describes the geometry of the components (e.g. 0-3, 2-2, 1-3, etc.). The 2-2 connectivity describes the bilayer structures, the 0-3 notation refers to the particle in a matrix composites, and 1-3 heterostructures are the vertical ones, with pillars embedded in a matrix.

I.2.1 Common materials for magnetoelectric thin films heterostructures

On the basis of structural and functional reasons, it has been proven beneficial to use perovskite ferroelectrics and magnetic spinels. Their study and usage has been motivated by the crystalline symmetry and individual properties.

I.3 Bismuth ferrite – $BiFeO_3$ (BFO)

Bismuth ferrite ($BiFeO_3$ – BFO) is the only multiferroic material at and above room temperature, with a ferroelectric order and an antiferromagnetic one. The unit cell is a rhombohedraly distorted perovskite, from the point group R3C, containing two distorted cubes connected along the diagonal ([111] pseudocubic axis) (figure I.3). The room temperature lattice parameter is a_{rh}=3.965Å and the rhombohedral angle is α_{rh}≈89.3-89.4°. The unit cell can also be described in a hexagonal frame, with the hexagonal axe *c* parallel with the perovskite cube diagonal ($[001]_{hexagonal} \| [111]_{pseudocubic}$), with the parameters a_{hex}=5.58Å and c_{hex}=13.9Å [57-59].

I.3.1 Ferroelectric properties

Bismuth ferrite is ferroelectric up to Curie temperature of T_C≈820°C, making it very attractive for applications. The electric polarization for bulk BFO is directed along the diagonal of the perovskite cube ($[111]_{pseudocubic}$ or $[001]_{hex}$) and the value is around 100 $\mu C \cdot cm^{-2}$. In thin films, the ferroelectric domain structure can be tuned through the synthesis process. The polarization has 8 variants that can be influenced by the symmetry of the substrate and it's electrical properties. [70]. Thus, relevant for the structures studied here, the interaction between BFO and $SrRuO_3$ lowers the number of variants, specially for the out-of plane polarization.

I.3.2 Magnetic properties

Bismuth ferrite is a G type antiferromagnetic (each F^{3+} is surrounded by 6 antiparallel spins of the closest Fe neighbours) with a Neel temperature of around 370°C. The spins do not align perfectly, they are canted due to the local coupling with the polarization. Besides this local structure, there is a cycloidal general structure with a 62-64 nm period, which propagates along the [110] direction [73,74]. The spins rotate in the plane determined by the cycloid direction and the polarization vector (figure I.5).

I.3.3 Electrical properties

The resistivity of bulk bismuth ferrite is over 10^{10} Ωcm [75,76], and it behaves as a semiconductor. The dielectric constant at room temperature in the GHz regime is around 30. Nevertheless, impedance measurements made usually in the 100Hz – 1MHz interval give bigger values (50 – 300), as a result of domain walls movement and charge accumulation [62].

I.3.4 Magnetoelectric properties

The linear magnetoelectric effect is suppressed by the presence of the spin cycloid, thus it would be expected to macroscopically observe higher order coupling effects. The behaviour of the magnetically induced electrical polarization (figure I.6) suggests that, after a critical field of about 20kOe, the magnetoelectric coefficient changes sign and becomes linear. This linear dependency on magnetic field implies that the spin cycloid vanishes.

I.4 Applications

The macroscopicall laminated heterostructures are viable mainly as magnetic field detectors, with the possibility of replacing the SQUID (superconducting quantum interference device). Their advantage resides in the fact that they don't need low temperature in order to operate.

At the nanoscale, the applications can be more varied, with the multi-functionality rising from the possibility of controlling magnetic and ferroelectric domains, domain walls, heterostructure interfaces, all of them having distinct electrical and magnetic properties.

Chapter II. Pulsed laser deposition of thin films

Pulsed laser deposition (PLD) is one of the most popular techniques for growing thin films. It is a vapour deposition technique which implies the interaction of a laser beam with a target of the desired material. The advantages of PLD are the ease of technical implementation, the stoichiometric transfer of the target's material on the substrate, flexibility in choosing the target etc. [79].

II.1 Target-laser interaction

The laser radiation is absorbed by the target and is transformed in thermal, chemical and mechanical energy. This will lead to evaporation, ablation and exfoliation. The formed plasma holds a mix of species, which can be atoms, molecules, ions and clusters, and is perpendicular to the target's surface. In order to avoid the presence of micron-sized particles in the plasma, the density of the target has to be high, thus limiting the volume energy transfer [80].

II.2 Thin film's growth modes

There are three general growth modes types: *i)* Volmer-Weber (tridimensional growth, or island type growth); *ii)* Frank-Van der Merwe (bidimensional, layer by layer growth); *iii)* Stranski-Krastanov (mixed growth) (figure II.3).

Volmer-Weber growth applies, for example, to metals on semiconductors on oxide substrates. Frank-Van der Merwe type is can be seen when epitaxially growing semiconductors and oxides. Stranski-Krastanov mechanism is a combination of the first two growth modes, and it applies for metal-metal and metal-semiconductor systems [84].

I.3 Mechanisms and theories concerning thin films' growth

Thin films form on the substrate through a process entailing nucleation and growth. During nucleation, growth centres (nuclei) appear on the substrate, which will become bigger and form layers during growth. The study of the process, both quantitatively and qualitatively, is a subject with many progresses in the past years.

II.3.1 Adsorption theory

This theory is based on the adsorption/desorption hypotheses formulated by Frenkel [79]. It states that the atoms reaching the substrate will stay there for a certain amount of time. During this time, if they don't loose all of their energy through diffusion on the substrate, they will be re-evaporated. Otherwise, they will form stability centres which will later form the film.

II.3.2 Thermodynamic theory

This theory states that, for the film to form, it is necessary to have growth islands consisting of a big number of particles. This entails an equilibrium state between the incident beam and the adsorbed atoms, which is hard to obtain in normal conditions, when the number of adsorbed atoms is smaller then the incident ones.

II.3.3 Atomic or statistical theory

Walter and Rhodin [85,86] developed a theory regarding the nucleation sites containing only a small number of atoms, in order to explain the epitaxial growth. This theory uses hypotheses from both of the theories described earlier. Thus, it is considered that, at low substrate temperatures or in supersaturation conditions, a crystallization nucleus can be made up of one atom, which by

randomly joining with another atom can become a stable centre, capable of growing further (adsorption theory). Similar to the thermodynamic theory, the centres' forming speed is proportional to the frequency of formation of nuclei with critical dimensions and their concentration.

II.4 Epitaxial growth

Epitaxial growth is defined as the growth of single crystal films on crystalline substrates. There are two types of epitaxy: homoepitaxy and heteroepitaxy. Homoepitaxy refers to growing a material on a substrate of the same material (e.g. doped Si on Si). Heteroepitaxy indicates that the substrate and the film are different materials, but have similar structures.

Chapter III. Experimental techniques

III.1 Atomic force microscopy

In the present study, the atomic force microscopy (AFM), together with it's additional modules, the piezoresponse force microscopy (PFM) and magnetic force microscopy (MFM), was vital for the local characterization of the thin films. At the nanoscale, this technique is indispensable for determining the quality of the samples. AFM is an imaging technique based on recording the interaction between the sample and a very thin tip. This tip is at the end of the free part of a cantilever, being brought in close proximity to the sample. The cantilever is bent by the interaction forces, which can be attractive or repulsive. Measuring the cantilever's deformation, given by Hooke's law ($F = -k \cdot \Delta x$, k – elastic constant of the cantilever and Δx – vertical displacement), and it's interpretation results in forming the image [87].

III.2 Scanning electron microscopy

Scanning electron microscopy (SEM) is one of the most versatile techniques in the analysis of thin films' morphology and chemical composition [89]. Image formation is given by acquiring the signal produced by the interaction of a electron beam and the sample. The useful information comes from the secondary electrons resulting from the ionization process which takes place at the surface of the sample (or very close to it). The penetration depth of the beam depends on the atomic number (density) of the material and the acceleration voltage.

III.3 Magnetocapacitance measurements

The direct magnetoelectric effect (the appearance of an electrical polarization when applying a magnetic field) can be revealed by measuring the capacitance variation in a magnetic field. The percentage variation is defined as follows:

$$\Delta C = \frac{C(H) - C(H = 0)}{C(H = 0)} * 100$$

For this analysis, it has to be taken into account that a magnetodielectric response is not necessary of magnetoelectric origin, but can be given by combination of Maxwell-Wagner (MW) effect and magnetoresistance [90,91]. The MW effect implies charge accumulation at the interface of two materials with different charge relaxation times.

III.4 Raman spectroscopy

Raman spectroscopy was used to determine the crystalline composition of the samples. This technique is based on the scattering of a monochromatic radiation, the photons being absorbed by the sample and emitted back with a different frequency. This technique was preferred to the X-ray diffraction (XRD) because there are studies that suggest the impossibility of distinguishing different types of ferrites through XRD [93,94].

Chapter IV. Alternative route for obtaining $NiFe_2O_4$ thin films by PLD

IV.1 Introduction

Nickel ferrite ($NiFe_2O_4$ - NFO) is a soft magnetic material with an inverse spinel structure. The ferrimagnetic character is given by the antiparallel orientation of the spins in the two sites of the material: tetrahedral (A, with Fe^{3+} ions) and octahedral (B, with Fe^{2+} and Ni^{2+} ions). The important properties of NFO giving it's applicability are: high Curie temperature (Tc~850K), low coercive field (Hc~250 Oe), high saturation magnetisation (M_S~300 emu/cc), high resistivity (ρ~1 kΩ·cm) etc. [97, 100,101]

$NiFe_2O_4$ thin layers can be obtained by various chemical and physical techniques [102-105]. Problems related to film quality, the complexity of the desired properties and/or limitations imposed by the applications, occur in all these methods [106]. Taking into account the advantages of pulsed laser deposition highlighted in chapter II, this method was chosen for this study. The aim was developing a process based on PLD for growing thin films of NFO with controlled phase distribution.

IV.2 Film deposition

Thin films of $NiFe_2O_4$ were obtained by PLD, with and without oxygen atmosphere. The classical route assumes the deposition in oxygen reactive atmosphere so that the desired stoichiometric material can be obtained. The deposition was done with a KrF excimer laser (λ=248 nm) with a fluence of about 5 $J \cdot cm^{-2}$. Table IV.1 holds the deposition conditions for the two set of samples.

Sample	Substrate	Conditions (temperature, pressure
F1	quartz	550°C, $3x10^{-6}$ mbar
F2	quartz	650°C, $2.5x10^{-6}$ mbar
F3	quartz	750°C, $4x10^{-6}$ mbar
F4	Si (001)	750°C, $4x10^{-2}$ mbar O_2

Table IV. 1 – Deposition conditions for $NiFe_2O_4$ thin films.

IV.3 Structural characterization

The composition of the crystalline phase was probed by Raman spectroscopy. First, the target was measured and the characteristic peaks of NFO where observed, without any secondary phases. The target was measured also after ablation, and only the characteristic response of magnetite was observed (Fe_3O_4).

The spectra for the F1-3 samples obtained in vacuum show only the presence of magnetite, similar to the target after ablation (figure IV.2). Sample F4 was made as a test sample, and the Raman spectrum (not shown here) is that of NFO.

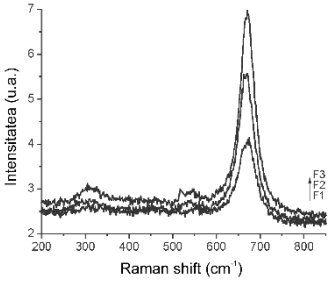

Figure IV. 1 – Raman spectra for the F1, F2 și F3 samnples.

The morphology of complex oxide thin films deposited by PLD depends on oxygen pressure and the substrate temperature. Using oxygen during deposition lowers the grain size by limiting the diffusion on the substrate through lowering the kinetic energy of the incident particles. It is also the case of our samples, as it can be seen figure IV.3. Also, a decrease in roughness is observed (~80nm (F3) to ~8nm (F4)). Temperature influence can be seen in the increase of the number of droplets and roughness [103], as is the case for our samples: F1 (4 nm), F2 (20 nm) and F3 (80 nm). It is interesting to note that the sample obtained in high vacuum at 550°C has a roughness comparable to the one deposited in oxygen atmosphere (at 750°C).

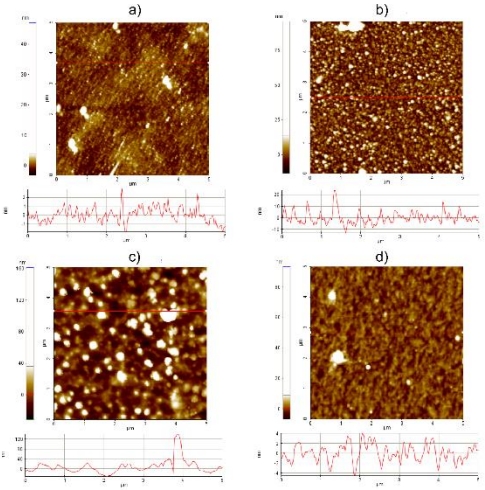

Figure IV. 2 –AFM images for the samples F1 (a), F2 (b), F3 (c) și F4 (d).

Obtaining the crystalline structure of magnetite after using a NFO target points to a high density of oxygen vacancies. XPS measurements (broad spectrum) were undertaken in order to test the presence Ni ions, and the results indicated the characteristic peaks for Ni 2p, Ni 3s and Ni 3p (figure IV.4). The presence of Ni was a good premise for attempting a phase transformation, similar in approach to annealing.

The new method for obtaining thin films of NFO implies the irradiation of the samples with an excimer laser (λ = 308 nm, pulse duration = 20 ns). To this

end, we used samples obtained at 750°C (F3 type). The irradiation was done at various frequencies (10, 25 and 50Hz), at low fluence (around 0,15 J·cm^{-2}) for 45000 and 90000 pulses. Table IV.2 holds the conditions for these processes.

Sample	Frequency (Hz)	Number of pulses (10^3)
F31	10	45
F32	25	45
F33	25	90
F34	50	90

Table IV. 2 – Irradiation conditions for the F3 type samples.

The result of this process is highlighted by Raman spectroscopy (figure IV.5). For the octahedral site, the characteristic peaks for NFO can be observed: 460 cm^{-1} – 660 cm^{-1} [109], indicating Ni ions integration in the crystalline structure and nickel ferrite formation. The signal from the tetrahedral site, situated at 690 cm^{-1}, does not correspond to NFO (704 cm^{-1}) nor to magnetite (670 cm^{-1}), so we can assume the coexistence of the two phases.

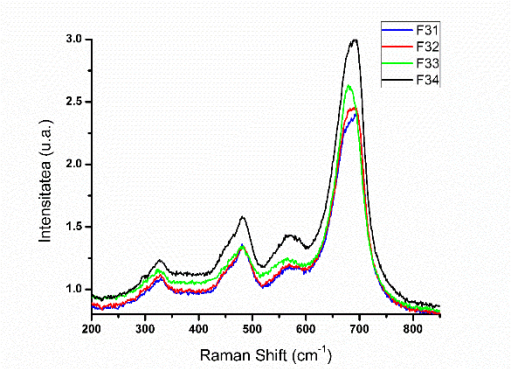

Figure IV. 3 – Raman spectra for the irradiated samples.

The morphological analysis, realised by AFM, shows that the roughness lowers after the process. The values for the samples F31, F32 and F34 are ~40 nm and for F33 it is ~ 20 nm (figure IV.6).

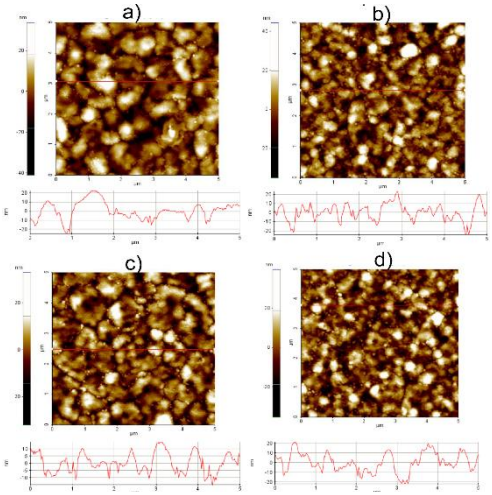

Figura IV. 4 – AFM images of the samples: F31 (a), F32 (b), F33 (c) and F34 (d).

In order to understand and optimize this effect, there is a need to further understand the thermal energy distribution and it's effect on oxygen vacancies. It can be observed that a high frequency (50 Hz) and a long irradiation time (90000 pulses) are beneficial for the phase change, but not for the roughness, when compared to a lower frequency (25 Hz) for the same time. Because residual magnetite is detected, we think that this process can be further optimized to obtain controllable ratios of the two materials (or similar ones) and thus tuneable magnetic and electrical properties.

Chapter V. Nanostructured multiferroic system $BiFeO_3$ – $CoFe_2O_4$

V.1 Introduction

The present study focused on growth and characterisation and characterization of vertical magnetoelectric heterostructures consisting of magnetic pillars embedded in a ferroelectric matrix. We aimed at developing a process that results in a highly ordered arrangement of the pillars. For this purpose we chose ferrimagnetic nickel ferrite ($CoFe_2O_4$ – CFO) and ferroelectric bismuth ferrite ($BiFeO_3$ – BFO).

Previous studies suggested that samples obtained by self-assembly present a certain hexagonal symmetry of the pillars in the matrix, given by substrate mediated strain interactions [13,113,114]. Thus, initially, such a sample was studied in order to find out the characteristic sizes of this symmetry. To this means, we analysed the autocorrelation image of the topography, which indicates the said symmetry, and the radially averaged autocorrelation function, from which the mean distance to the first neighbour ensues to be 285 nm (figure V.1) [115].

V.2 Synthesis method

We used a process based on self-assembly, to which we added an initial step of patterning the nucleation positions of the magnetic pillars, in order to induce the desired ordering. The schematics of the process is presented in figure V.2. The patterning was achieved using Au masks made by electron beam lithography (EBL) on the substrates. Through these masks, CFO islands were deposited to act as nucleation points. After the mask removal, the composite was

deposited from a mixed target. The mask parameters were chosen by taking into account the analysis results of the self-assembled sample.

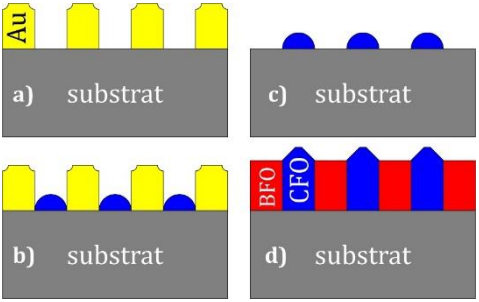

Figure V. 1 – Process schematics: a) Au mask transfer; b) CFO nucleation points deposition; c) mask removal; d) growth of the BFO-CFO system from a mixed target.

Before the mask transfer, $SrRuO_3$ (SRO) was deposited on (001) oriented $SrTiO_3$ (STO) to act as bottom electrode. Au masks were fabricated to have to symmetries: hexagonal and square. For both arrangements, two inter-pore distances (pitches) have been used: 200 nm and 300 nm. The pore diameter for all cases was kept constant at around 110 nm and the thickness at 50 nm (figure V.4).

The CFO islands were deposited through these masks (figure V.5) by means of PLD, with an excimer laser KrF (λ=248nm). Substrate temperature was

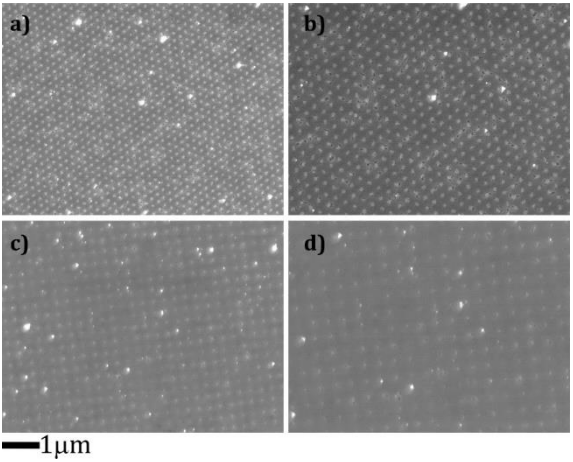

Figure V. 5 – SEM images of CFO nucleation points

kept constant at 600°C and oxygen pressure at 0.1 mbar. Based on deposition parameters, the height of the islands were estimated to be maximum 10 nm. After the deposition, the Au was chemically removed in a solution consisting 8 wt.% iodine, 21 wt.% potassium iodide and 71 wt.% distilled water.

The last step of the process was the deposition, from a mixed target of BFO-CFO (65%-35% molar ratio). Substrate temperature was kept at 650°C and oxygen pressure at 0.15 mbar.

V.3 Structural characterization

The SEM images of the results of nucleation induced self-assembly are presented in figure V.6. The best result is obtained for the 200 nm pitch. For the 300 nm pitch, the pillars present defects and additional pillars form outside the designated sites. This can be explained by bidimensional diffusion of the atoms on the substrate. Symmetry is also an important parameter. The hexagonal symmetry is optimum, as indicated also by the purely self-assembled sample.

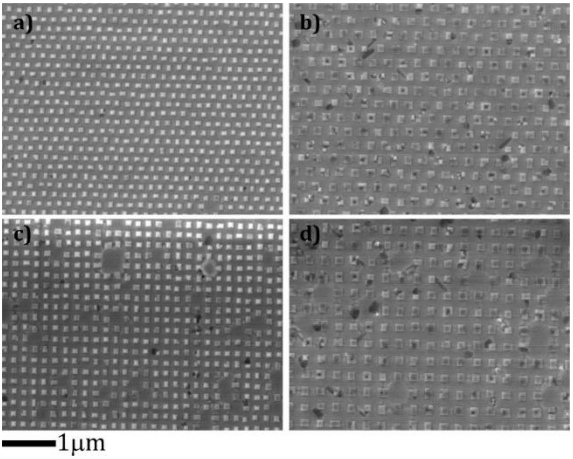

Figure V. 6 – SEM images of the BFO-CFO systems.

The sample obtained in optimum conditions (figure V.7 (a,b)) was further investigated. The morphology of a 1x1μm^2 area (figure V.8) shows the CFO pillars' height over the BFO matrix to be constant (65 nm) and the distribution of the pillars to be homogenous. From the phase image (figure V.8b), the pyramidal shape of the pillars stands out (figure V.8b).

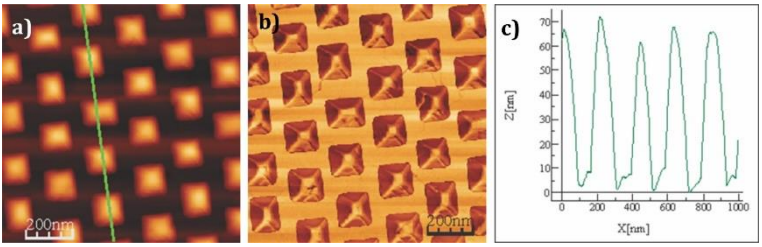

Figure V. 8 – Topography characterizations of the sample obtained in optimum conditions: a) amplitude and b) phase of the AFM scan; c) line profile drawn on (a).

Tilted SEM and TEM imaging were done for a better structure assessment (figure V.9). From the TEM image it follows that the pillars grow similar to the theoretical description and other experimental reports [1,7]. The outer surface is made up of (111) planes and a (001) plane on top. The thickness of the BFO film is around 55 nm, and the total height of the pillars is 120 nm. The thickness of the

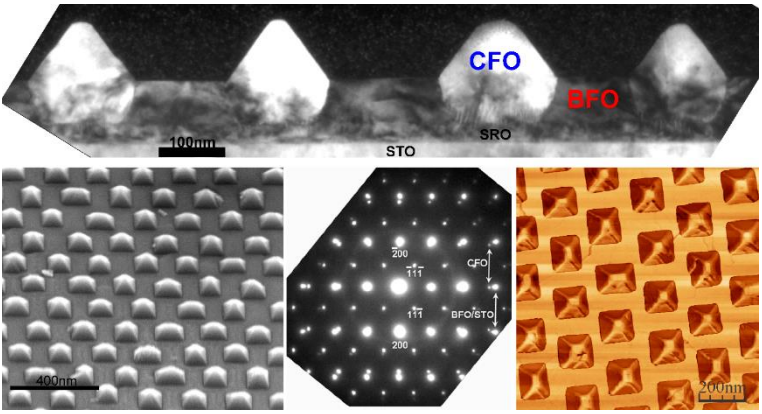

Figure V. 9 – a) TEM image of the optimum sample highlighting the pyramidal shape; b) 52° tilted SEM image; c) TEM diffraction pattern: reflection examples for CFO and BFO/STO marked by white arrows; SRO and STO have the reflexion in the same place ; d) AFM phase image showing complete phase segregation.

bottom SRO electrode is ~20 nm. The quality of the epitaxial growth can be seen from the diffraction pattern of the TEM, which demonstrates a cube-on-cube epitaxy.

Raman spectroscopy was used to determine the composition. The results are presented in figure V.10 along with the reference spectra for BFO and CFO. The response from the composite system has the 3 characteristic intervals [116]. At small wavenumbers, under 250 cm^{-1}, there are the three peaks of the BFO, which are sharp similar to the reference film, indicating a good crystallinity. At high wavenumbers, the characteristic peak of the CFO can be distinguished (695 cm^{-1}). The intermediary zone consists of the overlap of the two materials.

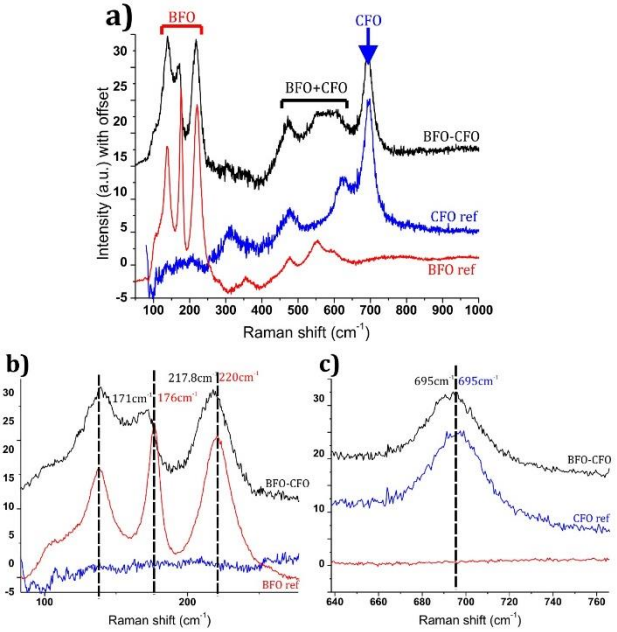

Figure V. 10 – a) Raman spectra of the BFO-CFO composite (black line), CFO reference (blue line) and BFO reference (red line); the intensity was modified and an offset was introduced to make the comparison clearer; b) zoom on BFO peaks; c) zoom on CFO peaks.

V.4 Functional characterization

Ferroelectric properties were analysed locally by means of PFM. The amplitude and phase are presented for a 1x1 μm^2 area (figure V.12). The ferroelectric response comes only from the BFO matrix. The amplitude of the piezoelectric response is homogenous and validates the segregation of the materials. The perpendicular response is almost uniformly indicating a polarization directed towards the substrate. The piezoelectric coefficient was determined from averaging several local measurements (d_{zz} vs. V_{ac}) and the value was found to be ~30 pm/V (figure V.13).

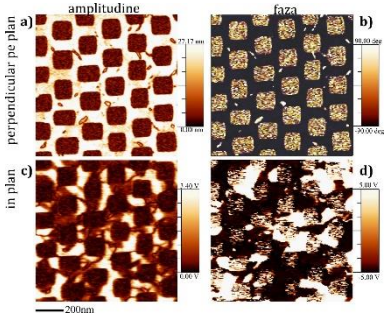

Figure V. 12 –PFM scanning on a 1x1 μm^2 area: a) amplitude and b) phase perpendicular to the film; c) amplitude and d) phase in-plane.

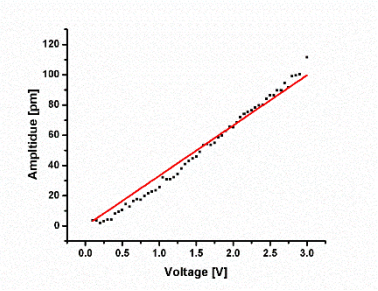

Figure V. 13 – Piezoelectric coefficient between 1 V și 3 V; red line is the fitting through zero.

The ferroelectric character was tested by locally measuring the phase and amplitude while varying the voltage between -4 V and 4 V. The result (figure V.14) clearly shows the hysteretic behaviour of both phase and amplitude, as expected from a ferroelectric material. The coercive voltage is measured to be ~±1V and the imprint is very small.

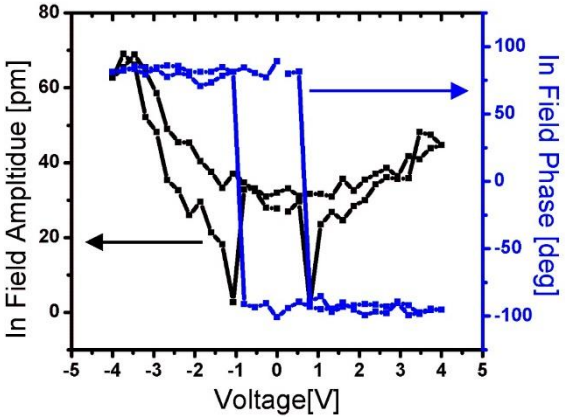

Figure V. 14 – Ferroelectric switching revealed through phase hysterezis curve and "butterfly-like" amplitude curve.

The magnetic force microscopy measurements show magnetic activity and no preferred magnetization orientation (figure V.15). The measurements' resolution is low, given the size of the MFM tip (radius of curvature ~70 nm), being close to the apex of the pillars.

V.5 Magnetoelectric coupling

The magnetoelectric coupling was tested via magnetocapacitance measurements. The parallel plate configuration was used, as shown in figure V.17. The top electrode was manufactured out of silver paste, with a diameter of ~0.3 mm. The magnetic field was applied perpendicular to the film and it was varied in the -80 kOe ÷ +80 kOe interval. The dc voltage applied to the sample had the amplitude of 0.6 V. The capacitance was measured with a E4980A precision LCR meter at four frequencies (1, 10, 100 and 1000 kHz) and four temperatures (10, 160, 200 and 260K). The assumed model was that of the parallel capacitance (C and a loss parallel resistor). This model is valid for high impedance samples, in the frequency interval that we used [92]. Table V.1 holds the measuring conditions.

T	f_{vac}	1kHz	10kHz	100kHz	1MHz

10K	$B \in (-80\ kOe, +80\ kOe)$ $\lvert V_{ac} \rvert = 0.6\ V$
160K	
200K	
260K	

Table V. 1 – Magnetocapacitance measurements' conditions.

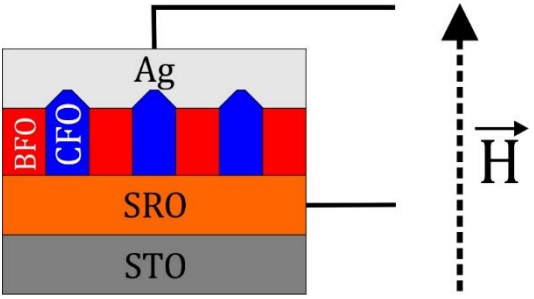

Figura V. 17 – Magnetocapacitance measurement system.

For the temperature of 10K, the capacitance vs. magnetic field is presented in figure V.18. At this temperature, one would expect the two materials to have very low conductivity and thus very low losses, leading to precise and valid measurements. The initial value of C_P, for B=0 kOe, is in the pF range, meaning a very high impedance. The unwanted influence of the combination of magnetoresistance with Maxwell-Wagner effect can be ruled out by the saturation of the magnetocapacitance and it's little variation with frequency. At high frequencies (1MHz), a certain change in behaviour and value can be observed. This can be attributed to the effect of the contacts series resistance. All measurements show an interval of quadratic dependence on the field (±25 kOe), and two linear intervals of similar slope.

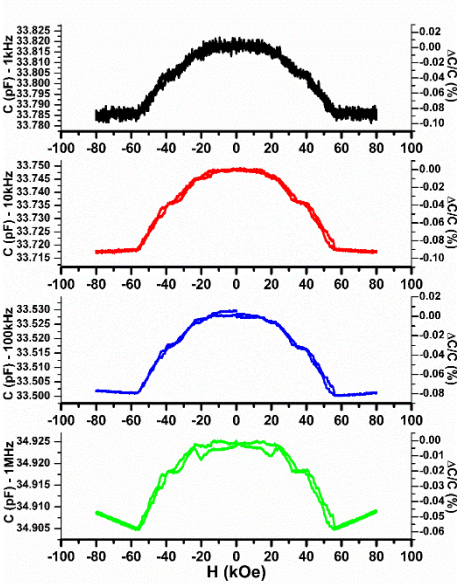

Figure V. 18 – Capacitance vs. magnetic field (absolute and relative values) at 10K.

The direct magnetoelectric effect implies the appearance of an electrical polarization when a magnetic field is applied. The magnetoelectric coupling coefficient can be related to the change in capacitance as follows:

$$\alpha \cdot H = \Delta C(H) \cdot \frac{V}{A}$$

Thus, the value of the coefficient can be determined from the slope of the magnetocapacitance variation. Using the two straight zones, the value of the coefficient was found to be ~0.6 and ~0.9 $\mu C/cm \cdot Oe$, respectively (figure V.19).

To validate the results and rule out any unwanted influences, the losses and their change in magnetic field have to be taken into account (figure V.20). At 1 kHz and 10 kHz, the losses are low and they do not vary more then 1.5%. At higher frequencies (100kHz and 1MHz), the losses are higher and their dependency in magnetic field is more clearly outlined as being hysteretic.

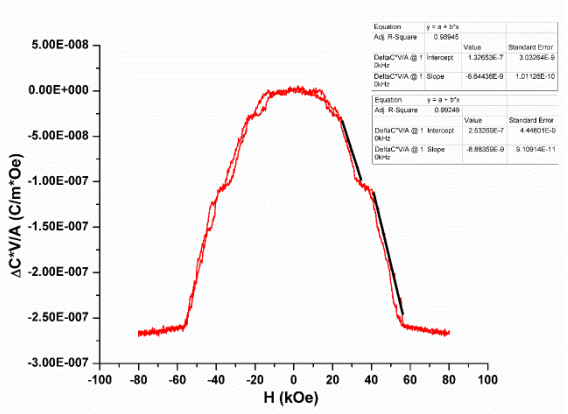

Figura V. 19 – Polarization induced by magnetic field; the two slopes represent the magnetoelectric coefficient.

At 160K, the capacitance value is similar to the one measured at 10K, but the variation is different. First of all it is clearly hysteretic. Second of all, there are sudden modifications (steps) of the capacitance (figure V.21), which appear for all frequencies at the same field values: 50 kOe, 70 kOe and 75 kOe. At fields lower than 20 kOe, the dependency seems quadratic, similar to the low temperature measurements. Also, the magnetocapacitance is independent on frequency, and the same type behaviour at 1MHz, as before, can be observed.

As expected, the losses for this temperature are higher than the previous case, but are still low (under 0.2). The hysteretic behaviour can be observed for the same frequencies (100kHz and 1MHz), but the percentage modifications are lower. At these frequencies, there are abrupt changes similar to those in capacitance (figure V.22).

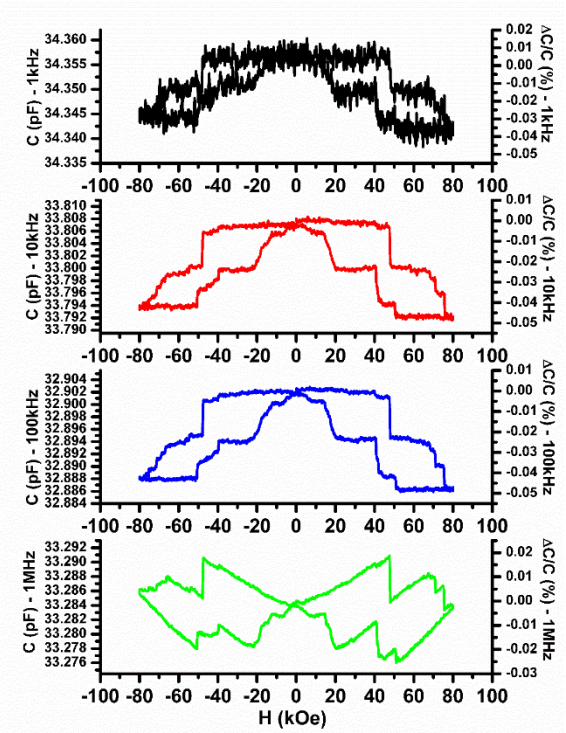

Figura V. 21 – Capacitance vs. magnetic field (absolute and relative values) at 160K.

The magnetocapacitance measured at 200K is also hysteretic and the steps appear at a bit lower magnetic fields, while the variation between the steps seems to be clearer (figure V.23). Under 20kOe, the magnetocapacitance is almost linear, compared to the quadratic behaviour observed at 160K. This can be a result of coercive field's inverse proportionality with temperature.

The losses do not rise significantly, in value or proportional changes, compared to the 160K case, but the variation in magnetic field is clearly different. This can suggest parasitic influences given by the magnetoresistance of the pillars.

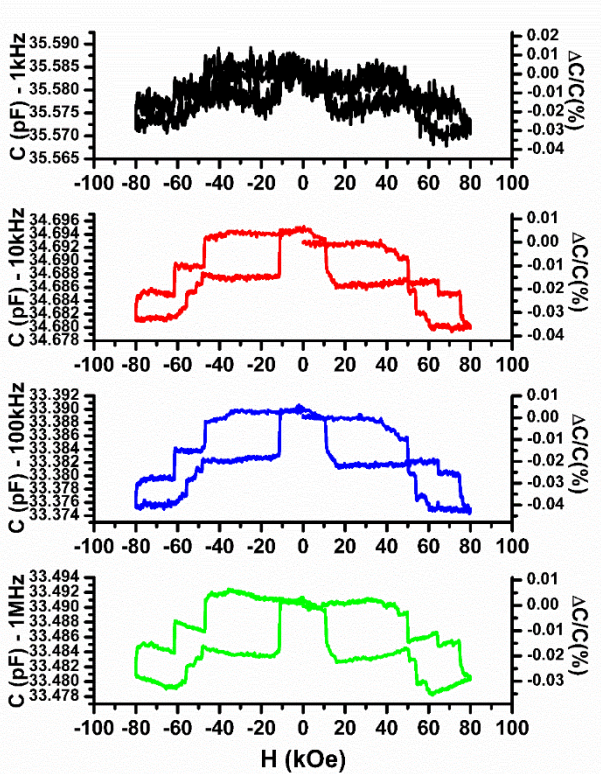

Figura V. 23 – Capacitance vs. magnetic field (absolute and relative values) at 200K.

Conclusions

The present study led to the development of a synthesis method for highly ordered vertical magnetoelectric heterostructures, based on PLD and self-assembly. Using Au masks for the deposition of the pillars' nucleation points, several arrangements, of different symmetries and parameters, were obtained. The subsequent deposition was done from a mixed target, similar to the self-assembly process. The structural characterisations show the success of the nucleation-induced self-assembly process. The optimum conditions involve a hexagonal symmetry with a mask inter-pore distance of 150 nm.

The functional investigations reveal ferroelectric properties of the BFO matrix to be similar to thin films, with low coercive voltage, small imprint and high piezoelectric coefficient. Local magnetic measurements show magnetic activity, but the low resolution doesn't allow to clearly differentiate between the magnetic domains in a pillar.

Magnetoelectric coupling is shown at various temperatures by means of magnetocapacitance measurements. The validity of the results is supported by the small value of losses and the small influence of frequency.

An additional study on nickel ferrite thin films revealed a new process for the synthesis of nickel ferrite thin films by laser irradiation of magnetite films with nickel inclusions. Compositional analysis shows the presence of both NFO and magnetite in the resulting samples. The influence of several parameters on morphology is shown.

Selective bibliography

[5] P. Curie, *J. Physique*, **1894**, *3*, 393.

[6] P. Debye, *Z. Phys.*, **1926**, *36*, 300.

[7] L. D. Landau and E. M. Lifshitz, *Electrodynamics of continuous media* (Fizmatgiz, Moscow, **1959**).

[8] I. E. Dzyaloshinskii, *Sov. Phys. – JETP*, **1959**, *10*, 628.

[9] D. Astrov, *Sov. Phys. – JETP*, **1960**, *11*, 708.

[10] I.F. Martinez, *Ferroelectricity and magnetoelectric coupling in magnetic ferroelectrics and artificial multiferroic heterostructures*, (Barcelona, **2012**).

[11] N. A. Hill, *The Journal of Physical Chemistry B*, **2000**, *104*, 6694.

[12] J. Wang, J. B. Neaton, H. Zheng, V. Nagarajan, S. B. Ogale, B. Liu, D. Viehland, V. Vaithyanathan, D. G. Schlom, U. V. Waghmare, N. A. Spaldin, K. M. Rabe, M. Wuttig, and R. Ramesh, *Science*, **2003**, *299*, 1719.

[13] H. Zheng, J.Wang, S. E. Lofland, Z. Ma, L. Mohaddes-Ardabili, T. Zhao, L. Salamanca-Riba, S. R. Shinde, S. B. Ogale, F. Bai, D. Viehland, Y. Jia, D. G. Schlom, M. Wuttig, A. Roytburd, and R. Ramesh, *Science*, **2004**, *303*, 661.

[14] B.D.H. Tellegen, *Philips Res. Rep.*, **1948**, *3*, 81.

[15] J. van Suchtelen, *Philips Res. Rep.*, **1972**, *27*, 28.

[39] M. Fiebig, T. Lottermoser, D. Frohlich, A.V. Goltsev, and R.V. Pisarev, *Nature*, **2002**, *419*, 818.

[40] Y.-H. Chu, L.W. Martin, M.B. Holcomb, M. Gajek, S.-J. Han, Q. He, N. Balke, C.-H. Yang, D. Lee, W. Hu, Q. Zhan, P.-L. Yang, A. Fraile-Rodríguez, A. Scholl, S. X. Wang and R. Ramesh, *Nature Materials*, **2008**, *7*, 478.

[43] L. Mitoseriu and V. Buscaglia, *Phase Transitions*, **2006**, *79*, 1095.

[44] G. Harshe, J.P. Dougherty and R.E. Newnham, *Proc. SPIE*, **1973**, *1919*, 224.

[53] F. Zavaliche, H. Zheng, L. Mohaddes-Ardabili, S. Y. Yang, Q. Zhan, P. Shafer, E. Reilly, R. Chopdekar, Y. Jia, P. Wright, D. G. Schlom, Y. Suzuki and R. Ramesh, *Nano Letters*, **2005**, *5*, 1793.

[60] V.M. Goldschmidt, *Naturwissenschaften*, **1926**, *14*, 477.

[62] G. Catalan, J. Scott, *Advanced Materials*, **2009**, *21*, 2463–2485.

[66] J. Li, J. Wang,M.Wuttig, R. Ramesh, N. Wang, B. Ruette, A. P. Pyatakov, A. K. Zvezdin, D. Viehland, *Appl. Phys. Lett.*, **2004**, *84*, 5261.

[70] F. Johann, A. Morelli, D. Biggemann, M. Arredondo, I. Vrejoiu, *Physical Review B,* **2011**, *84*, 1–10.

[78] J.F. Scott, *Journal of Materials Chemistry*, **2012**, *22*, 4567.

[79] Robert Eason, *Pulsed Laser Deposition of Thin Films – Applications-led Growth of Functional Materials* (Ed. Wiley, **2007**).

[86] R.N. Rodin and D. Walter, *Single crystal films*, (ed. Francombe, H. Maurice and H. Sato, Pergamon Press, N.Y. **1964**).

[88] Alessio Morelli, *Piezoresponse Force Microscopy of Ferroelectric Thin Films* (University of Groningen, Zernike Institute OhD thesis series 2009-12, **2009**).

[89] Weilie Zhou, Zhong Lin Wang, *Scanning Microscopy for Nanotechnology Techniques and Applications* (Springer Science+Business Media, LLC, **2006**).

[90] G. Catalan, *Applied Physics Letters*, **2006**, *88*, 102902.

[92] Agilent, *Agilent Impedance Measurement Handbook* (edited by I. Agilent Technologies, Agilent Technologies, Inc., **2009**).

[96] Peter Larkin, *Infrared And Raman Spectroscopy Principles And Spectral Interpretation* (Elsevier Inc., **2011**).

[110] H. Zheng, F. Straub, Q. Zhan, P.-L. Yang, W.-K. Hsieh, F. Zavaliche, Y.-H. Chu, U. Dahmen, R. Ramesh, *Advanced Materials*, **2006**, *18*, 2747–2752.

[111] H. Zheng, J. Wang, L. Mohaddes-Ardabili, M. Wuttig, L. Salamanca-Riba, D.G. Schlom, R. Ramesh, *Applied Physics Letters*, **2004**, *85*, 2035.

[112] R. Comes, H. Liu, M. Khokhlov, R. Kasica, *Nano Letters*, **2012**.

[113] M. Dawber, I. Szafraniak, M. Alexe, J.F. Scott, *Journal of Physics: Condensed Matter*, **2003**, *15*, L667–L671.

[114] J. Slutsker, Z. Tan, A. Roytburd, I. Levin, *J. Mater. Res.*, **2007**, *22*, 2087–2095.

[117] F. Johann, A. Morelli, D. Biggemann, M. Arredondo, I. Vrejoiu, *Physical Review B*,**2011**, *84*, 1–10.

Communications and publications list:

1. *„Alternative route for obtaining NiFe2O4 by PLD"*, Sergiu M Stratulat, Cristian Ursu, Ovidiu Florin Călțun, **9th European Conference on Magnetic Sensors and Actuators**, 1-4 Iulie 2012, Praga, Cehia; tipul comunicării: poster;

2. *„Nucleation-induced self-assembly of nanostructured BiFeO3-CoFe2O4",* Sergiu M Stratulat, Dietrich Hesse, Marin Alexe, **Deutsche Physikalische Gesellschaft**, 10-15 Martie 2013, Regensburg, Germania; tipul comunicării: prezentare orală;

3. *„Nucleation-induced self-assembly of nanostructured BiFeO3-CoFe2O4",* Sergiu M Stratulat, Dietrich Hesse, Marin Alexe, **WG1 Workshop "Nanoscale phenomena" & Core Group meeting**, 18-22 Martie 2013, Belfast, U.K.; tipul comunicării: prezentare orală;

- *„Alternative route for obtaining $NiFe_2O_4$ by PLD"*, Sergiu M Stratulat, Cristian Ursu, Ovidiu Florin Călțun, **IEEE Transactions on Magnetics, vol. 49, no. 1, january 2013.**

„Nucleation-Induced Self-Assembly of Multiferroic BiFeO3–CoFe2O4 Nanocomposites", Sergiu M. Stratulat, Xiaoli Lu, Alessio Morelli, Dietrich Hesse, Wilfried Erfurth, and Marin Alexe, **Nano Letters, 2013, dx.doi.org/10.1021/nl401965z.**